

pubs.acs.org/Macromolecules Article

Quasicrystals and Their Approximants in a Crystalline-Amorphous Diblock Copolymer

Andreas J. Mueller, Aaron P. Lindsay, Ashish Jayaraman, Timothy P. Lodge, Mahesh K. Mahanthappa,* and Frank S. Bates*

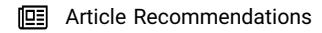


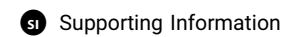
Cite This: Macromolecules 2021, 54, 2647-2660



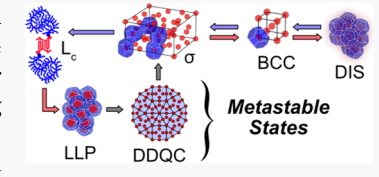
ACCESS

Metrics & More





ABSTRACT: Discoveries of Frank–Kasper phases and closely related dodecagonal quasicrystals (DDQCs) in soft, mesoscopic systems have galvanized efforts to unveil the fundamental mechanisms that drive the formation of these remarkably complex micellar packings. Toward this end, we report temperature-dependent small-angle X-ray scattering analyses of a crystalline–amorphous poly(ethylene oxide)-block-poly(2-ethyl hexylacrylate) (OA) diblock copolymer with $M_{\rm n}=8300$ g/mol, $D=M_{\rm w}/M_{\rm n}=1.10$, and volume composition $f_{\rm O}=0.21$. On heating at ambient temperature, this polymer assembles sequentially into five



distinct morphologies prior to melt disordering at $T_{\rm ODT}$ = 69 °C: semicrystalline lamellae (L_c), a liquid-like packing (LLP) of particles lacking translational order, an aperiodically ordered DDQC, a periodic FK σ phase, and a body-centered cubic (BCC) packing of particles. Detailed investigations of thermal processing conditions that foster DDQC formation reveal that this metastable morphology only forms in melts exhibiting LLP characteristics arising from either melting the L_c phase at low temperature or quenching a high-temperature disordered state, and that this DDQC eventually evolves into a σ approximant phase. Cooling a well-ordered BCC phase induces direct formation of a σ phase with no evidence of DDQC formation, suggesting the critical importance of particle size distribution of the disorganized yet segregated LLP state in triggering the emergence of a DDQC.

■ INTRODUCTION

Self-assembled soft materials furnish a robust platform for investigations of the fundamental geometric principles underlying the organization of discrete particles into periodic crystals. These particles, comprising tens to hundreds of individual molecules, form micellar arrangements with unit cells that span orders of magnitude in length scale. These range from sub-10 nm unit cells in electrostatically organized ionic surfactant dispersions in water²⁻⁴ to 100 nm unit cells of block polymer micelles governed by van der Waals interactions.⁵⁻⁸ A recent renaissance in the study of particle packings was stimulated by discoveries of mesoscopic Frank-Kasper (FK) phases in soft materials. The FK phases are tetrahedrally-close packed (TCP) structures conforming to the paradigm developed for transition metal alloys in the 1950s by Frank and Kasper. 9,10 They are constructed from icosahedral 12-fold coordination motifs, which are locally the most efficient means of packing tetrahedral atomic clusters, yet are only capable of periodically tessellating space in conjunction with supplemental higher order 14-, 15-, or 16-coordination environments. In self-assembled soft particle packings, such heterogeneity in local packing mandates the formation of multimodal distributions of discrete particle sizes and shapes reflecting the underlying lattice symmetry. This phenomenon conflicts with the conventional wisdom that simple, highsymmetry lattices comprising a single coordination environment such as a body-centered cubic (BCC) packing are

The 2010 discovery of a FK σ phase (P4₂/mnm space group symmetry), in which 30 particles of five symmetry-equivalent classes order into a large tetragonal lattice, in a 1,4poly(isoprene)-block-poly(DL-lactide) (IL) melt marked the induction of diblock copolymers into the growing class of FK phase-forming micellar soft materials. 11 To date, FK phases have been observed in "normal" (type I) and "inverse" (type II) lyotropic liquid crystals of minimally hydrated surfactants, 2,3,12,13 molecularly complex dendrimers, 14-16 giant shape amphiphiles, ^{17–19} multiblock copolymers, ²⁰ and block polymer blends. 5-8 Diblock copolymers, which constitute the simplest and most theoretically tractable of these systems, are well described by just three parameters: (i) the volume fraction of one block (f_A) , (ii) the segregation strength (χN) , as an aggregate of the total volumetric degree of polymerization (N)and the inter-segment interaction parameter $\chi \sim T^{-1}$, and (iii) the conformational asymmetry, $\varepsilon = (b_A/b_B)^2$, which captures differences in the statistical segment lengths b_A and b_B of the component blocks with respect to a common reference volume.^{21–25}

Received: December 29, 2020 Revised: February 9, 2021 Published: March 3, 2021





In 2016, Gillard et al. demonstrated that rapidly quenching the fluctuating disordered state (DIS) of a σ phase-forming IL diblock copolymer melt leads to two-dimensional aperiodic order through dodecagonal quasicrystal (DDQC) formation.²⁶ As in the case of periodic FK phases, this discovery in diblock copolymers complemented early and scattered reports of soft DDQCs^{27–29}—led by the seminal discovery of Zeng et al.³⁰ and augmented them by continued identification, 18,20 particularly in linear diblock copolymer systems.^{6,31} Quasicrystals, which are widely documented in metal alloys,^{32–34} are aperiodically ordered materials that lack translational symmetry while exhibiting local rotational symmetry, such as the 126screw axis characteristic of a DDQC. 35,36 Recent observations of such soft quasicrystals offer enticing opportunities to explore the fundamental origins of aperiodic order across a wide range of materials. The fact that DDQCs are typically found near FK σ and A15 phases is no coincidence, as the latter structures are periodic approximants to DDQCs. 37,38 In other words, all three states comprise the same local particle cluster motifs and are distinguished only by the extent and symmetry of their mesoscale order. Therefore, the mechanisms that stabilize these structures are ostensibly intertwined. While quantitative theories for periodic FK phase formation in soft materials and particularly diblock copolymer melts have been established, ^{39–41} general conditions that enable DDQC formation and the means by which they do so remain obscure.

Conformational asymmetry is a key molecular parameter that stabilizes FK phases in neat diblock copolymer melts.^{23–25} Particles with $f_{\text{core}} \lesssim 0.40$ undergo spontaneous symmetry breaking to assume a multimodal particle size distribution *via* a local particle shape optimization mechanism.³⁹ This phenomenon stems from the fact that densely packed micelles sacrifice an optimally spherical shape in order to fill space at constant density, assuming instead polyhedral forms that encode the lattice symmetry known as Wigner-Seitz (WS) cells. 42-46 Micelle corona faceting, when transmitted to the particle cores at modest f_{core} , produces additional interfacial contact area (enthalpy) and chain stretching entropy penalties that are relieved by assuming optimal particle shapes characteristic of FK-phase WS cells. ^{39,40} In order to broaden the palette of conformationally asymmetric monomer pairs that form complex particle packings, we sought to investigate the morphologies of a conformationally asymmetric poly(ethylene oxide)-block-poly(2-ethyl hexyl acrylate) (OA) diblock copolymer (Figure 1) that forms particles with poly(ethylene oxide) (O) cores.

Kim et al. established the importance of the segregated particle size distribution in symmetry selection among nearly energetically degenerate FK phases. 41,47 They demonstrated that specific thermal processing protocols offer access to particle size distributions that form Laves-type FK phases. In a BCC-forming melt, Takagi et al. recently established that block crystallization in 1,4-poly(butadiene)-block-poly(ε -caprolactone) with $f_{\rm CL}$ = 0.18 offers a complementary means of tailoring the particle size distribution that guides microphaseseparated structure formation.⁴⁸ This result reflects the fact that segment crystallization in crystalline-amorphous (CA) diblock copolymers usually leads to disruption ("break out") of the segregated melt morphologies to yield lamellar phases (L_c) comprising alternating semicrystalline and amorphous layers, regardless of composition, when the melt segregation strength and amorphous layer glass transition temperature present only minimal kinetic barriers. $^{49-52}$ Thus, we further sought to assess

poly(ethylene oxide-block-2-ethyl hexyl acrylate) (OA)

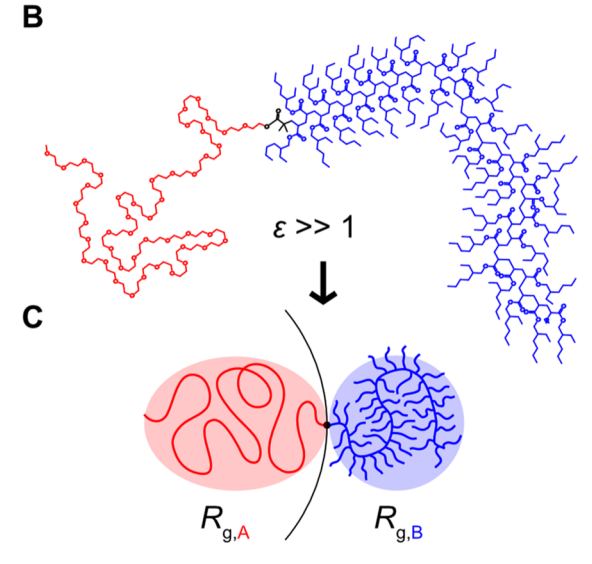


Figure 1. (A) Structure of OA. (B) Illustration of the OA21 diblock utilized in this study. (C) Schematic of the OA21 diblock demonstrating the effects of large conformational asymmetry (ε) on interfacial curvature, visualized through differences in the pervaded volume of each segment (*filled ovals*) that scales with the block radii of gyration ($R_{\rm g,A}$ and $R_{\rm g,B}$).

whether the semicrystalline O core domains of OA diblocks offer an additional means of tailoring the particle size distributions to favor periodic FK-phase selection or aperiodically ordered DDQC formation.

Herein, we describe the phase behavior of an OA diblock polymer molecularly designed to disorder on heating and to disorder on cooling due to O crystallization breakout. Smallangle X-ray scattering (SAXS), differential scanning calorimetry (DSC), and polarized light microscopy (PLM) analyses of this OA material at ambient temperature reveal the formation of a L_c morphology. Temperature-dependent SAXS studies demonstrate the formation of DDQC, σ , and BCC packings on heating prior to an order-to-disorder transition at $T_{\rm ODT} \approx 69$ °C. Using various thermal processing strategies, including directly melting the semicrystalline L_c state, quenching a thermally DIS, and quenching an ordered BCC structure, we identify conditions that lead to formation of DDQCs. These studies indicate that DDQCs nucleate prior to equilibrium σ phase formation only in cases where the preceding structure is a micellar liquid. Furthermore, DDQCs do not form as intermediates in the cooling-induced transition of a BCC phase into an equilibrium σ phase. By analogy to earlier work by Jayaraman et al.,53 we rationalize this behavior in terms of the shape of the underlying particle size distribution of the melt, invoking Ostwald's step rule 54,55 to rationalize the development of a metastable aperiodic order during the crystallization of a micellar liquid.

■ EXPERIMENTAL METHODS

Materials. All reagents were purchased from Sigma-Aldrich Chemical Co. (Milwaukee, WI). Triethylamine (Et₃N), α-bromoisobutyryl bromide, and N_1,N_1,N_1,N_1,N_1,N_1 -pentamethyldiethylenetriamine (PMDETA) were each stirred with calcium hydride (CaH₂) overnight, distilled under vacuum, and stored under nitrogen. Poly(ethylene glycol) methyl ether (PEO–OH; nominally, 2000 g/mol) was azeotropically freeze-dried with benzene and stored under argon. CuBr was purified by a literature procedure. See 2-Ethylhexyl acrylate was stirred with Brockman type I basic alumina for 1 h under ambient conditions and gravity-filtered in order to remove inhibitors prior to use. Anhydrous CH₂Cl₂ was obtained from a Vacuum Atmospheres Co. (Hawthorne, CA) solvent purification system. Anhydrous N_1,N_2 -dimethylformamide (DMF) and CuBr₂ were used as received.

Nuclear Magnetic Resonance Spectroscopy. $^1\mathrm{H}$ nuclear magnetic resonance (NMR) spectra were acquired on a Bruker Avance II HD 400 MHz spectrometer in CDCl3. Spectra for polymer samples were acquired using a pulse repetition delay of >15 s to enable quantitative integration for composition analyses. All spectra were referenced to the residual protiated solvent resonance (δ 7.26 ppm).

Size Exclusion Chromatography. Molar mass (M_n) and molar mass dispersity $(D = M_w/M_n)$ were determined by size exclusion chromatography (SEC) conducted on a system equipped with two Agilent Polypore columns and a Wyatt Dawn Heleos II light scattering detector. Butylated hydroxytoluene-stabilized tetrahydrofuran (THF) was used as the mobile phase at a flow rate of 1 mL/min. A weight-averaged refractive index increment $\partial n/\partial c$ was employed in the total molecular weight (M_w) measurement for the diblock using $(\partial n/\partial c)_O = 0.068$ mL/g and $(\partial n/\partial c)_A = 0.072$ mL/g for the poly(ethylene oxide) and poly(2-ethyl hexylacrylate) segments, respectively. Signature of the signature of the segments of the poly(ethylene oxide) and poly(2-ethyl hexylacrylate)

Matrix-Assisted Laser Desorption/Ionization Time-of-Flight Spectrometry. The molar mass $(M_{\rm n})$ and molar mass dispersity $(D=M_{\rm w}/M_{\rm n})$ of the PEO-OH precursor were verified via matrix-assisted laser desorption/ionization-time of flight spectrometry (MALDI-ToF) analyses conducted on an AB Sciex 5800 MALDI-ToF/ToF mass spectrometer in the reflectron-positive ionization mode. Samples were prepared directly on sample plates using an α -cyano-4-hydroxycinnamic acid matrix and approximately 0.5 μ L of a 50:50 volume acetonitrile/water solution with 1 vol % trifluoroacetic acid

Synthesis of a PEO-Br Macroinitiator (PEO-Br). PEO-OH (15 g, $M_{\text{n,NMR}} = 1980 \text{ g/mol}$, $M_{\text{n,MALDI}} = 1917 \text{ g/mol}$, and D = 1.03) was dissolved in CH2Cl2 (100 mL) in a 250 mL Schlenk flask under nitrogen. The reaction flask was cooled to 0 °C and excess Et₃N (2.5 equiv per -OH end group, 18.75 mmol, 2.63 mL) was added, followed by excess α -bromoisobutyryl bromide (2.2 equiv per -OHend group, 16.5 mmol, 2.04 mL). The cooling bath was removed, and the reaction mixture was allowed to warm to ambient temperature and to stir overnight. Following solvent removal from the resulting black reaction mixture via rotary evaporation, the solids were dissolved in benzene (20 mL), filtered through Brockman type I basic alumina packed into a medium frit, and the filtrate was poured into hexanes (500 mL). Solids isolated from this precipitation were redissolved in C₆H₆ (20 mL) and reprecipitated into hexanes (500 mL) a second time. The resulting white paste was freeze-dried with benzene and stored in a glove box under argon. Complete end functionalization was verified through ¹H NMR (400 MHz, CDCl₃, 24 °C): δ (ppm) 4.35 (m, 2H, int: 1.97), 3.86–3.47 (m, 176H), 3.40 (s, 3H, int: 3.00), 1.97 (s, 6H, int: 6.02) from which one obtains $M_{\rm n,NMR}$ = 2100 g/mol.

Synthesis of OA Diblock. A mixture of 2-ethylhexylacrylate (42 mL, 202 mmol), PMDETA (253 μ L, 1.21 mmol), CuBr₂ (22.6 mg, 0.10 mmol), and DMF (8.42 mL, 109 mmol) was added to an ovendried 250 mL Schlenk flask. This mixture was subjected to three freeze—thaw degassing cycles, during the third of which CuBr (153 g, 1.08 mmol) was added under positive nitrogen pressure. The flask

was then evacuated and thawed a final time prior to stirring at 45 °C for 1 h to ensure that all components completely dissolved to yield a homogeneous teal-colored mixture. An aliquot of this mixture (9.2 mL) was then transferred to a 50 mL Schlenk tube charged with PEO-Br (380 mg, 0.18 mmol) under nitrogen at ambient temperature. Polymerization was initiated by plunging the Schlenk tube into an oil bath at 70 °C and allowing it to react for 35 min. The polymerization was halted by immersing the reaction tube in a beaker of ice water, followed by opening it to air and diluting it with CH3OH (10 mL). This mixture was further diluted with CH₂Cl₂ (20 mL) prior to filtering it through Brockman type I basic alumina packed in a medium frit. The filtrate was concentrated by rotary evaporation and precipitated dropwise into stirred acetone at −78 °C. Residual solvent was removed from the isolated polymer under vacuum prior to freezedrying the diblock from benzene. $M_{n,SEC} = 9400$ g/mol, D = 1.11 by SEC in THF, and $M_{n,NMR}$ = 8300 g/mol, and f_O = 0.21 by quantitative ¹H NMR spectroscopy.

Differential Scanning Calorimetry. DSC analyses employed a TA Instruments Q1000 DSC. The samples (\sim 5 mg) were placed in hermetically sealed aluminum TZero DSC pans (DSC Consumables, Austin, MN) under air. The samples were cooled to $-100~^{\circ}$ C and then heated to $100~^{\circ}$ C at $10~^{\circ}$ C/min, and this cycle was repeated twice. Reported data originate from the second heating and cooling ramps.

Small-Angle X-ray Scattering. SAXS experiments were performed at the Advanced Photon Source at Argonne National Lab (Argonne, IL). Prior to SAXS analyses, all samples were freezedried from C₆H₆ and loaded into hermetically sealed aluminum TZero DSC pans (DSC Consumables, Austin, MN) under argon. Temperature-dependent synchrotron SAXS was carried out either at the sector 12-ID-B beamline using $\lambda = 0.886$ Å with a Pilatus 2 M detector with 1475×1679 resolution of $172 \times 172 \mu m$ pixels over an area of 253.7 \times 288.8 mm² or at the sector 5-ID-D beamline using λ = 0.7293 Å with a Rayonix MX170-HS detector with a 3840 × 3840 resolution of 86.6 \times 86.6 μ m pixels over an area of 170 \times 170 mm². Temperature control was afforded by a Linkam hot stage (±1 °C temperature accuracy) in both cases. For extended sample annealing experiments, annealing was performed on thermostatted hot plates from which the samples were rapidly transferred to the pre-heated Linkam hot stage. Patterns were calibrated using either silver behenate (d = 58.37 Å) at sector 12 or an Au-coated Si grating (7200 lines/ mm) at sector 5. 2D SAXS patterns were azimuthally integrated to produce one-dimensional intensity I(q) versus scattering wave vector magnitude $q = |q| = 4\pi\lambda^{-1} \sin (\theta/2)$ using the software available at each beamline.

Polarized Light Microscopy. PLM experiments were conducted on an Olympus BX53 Upright Microscope equipped with Olympus U-pot and U-AN360P polarizers and an Olympus U-PCD2 phase contrast condenser. Fine temperature control was afforded by a Linkam LTS240 temperature control stage with images captured using a QICAM Fast 1394 camera. In order to further increase image contrast, a differential interference contrast full-wave plate (Olympus U-P521) was also employed. The samples were prepared by sandwiching a small amount of diblock copolymer (1–5 mg) between a glass slide and a coverslip.

■ RESULTS AND ANALYSIS

Synthesis and Molecular Characterization of OA21.

This study focuses on a model particle-forming OA diblock copolymer with a minority O block ($f_{\rm O}$ < 0.50). The poly(2-ethyl hexyl acrylate) (A) corona block was selected in order to stabilize a wide window of point particle phases with O core domains, by virtue of the expected high degree of conformational asymmetry of the O/A monomer pair. Using packing length arguments developed by Fetters $et~al.^{58}$ in concert with the A homopolymer entanglement molecular weight ($M_{\rm e}\approx 60~{\rm kg/mol})^{50}$ and the statistical segment length for O, ⁴⁹ the conformational asymmetry for this monomer pair is estimated

to be $\varepsilon \approx 3.5$ (see the Supporting Information for detailed estimation). ⁵⁹

Cu-catalyzed atom transfer radical polymerization⁶⁰ of 2ethylhexyl acrylate initiated from a PEO-Br macroinitiator, which was derived from end functionalization of a semitelechelic α-hydroxy O homopolymer, 61 yielded a compositionally asymmetric OA diblock copolymer. The OA21 diblock described here exhibits $f_{\rm O}$ = 0.21 with total $M_{\rm n,NMR}$ = 8300 g/ mol and D = 1.11, which corresponds to a segment density normalized degree of polymerization of N = 124 relative to a 118 Å³ reference volume. Representative MALDI-TOF MS, ¹H NMR, and SEC characterization of the O homopolymer precursor, PEO-Br, and OA21 are presented in Figures S1-S5. In view of the narrow molar mass dispersity $D_0 = 1.03$ measured by MALDI-MS for the O core segment with $M_{n,O}$ = 1980 g/mol, we surmise that the broader overall D of OA21 stems from A-segment dispersity. Assuming that the constituent segment dispersities are statistically uncorrelated, we estimate $D_A = 1.19$ (see the Supporting Information for calculation details).⁶² In contrast to previous studies of particle-forming systems with poly(lactide) cores, this slightly broader DA is expected to destabilize the FK phases in OA diblocks due to dispersity-induced shifts in the ordered phase boundaries. 6,47,63 Nonetheless, the following findings establish that particle packings of low N, high ε diblock systems are independent of constituent segment chemical identities.

Thermal Characteristics of OA21. The thermal transitions of OA21 were probed *via* DSC at a ramp rate of 10 °C/min in the second heating and cooling thermograms given in Figure 2. The broad, low-temperature change in polymer heat

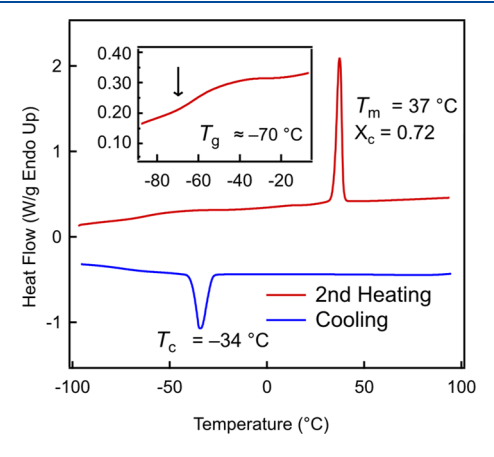


Figure 2. DSC thermogram of OA21 displaying glass transition at $T_{\rm g} \approx -70$ °C (inset) alongside melting $(T_{\rm m})$ and crystallization $(T_{\rm c})$ endotherms and exotherms.

capacity is indicative of a glass transition temperature $T_{\rm g} \approx -70~^{\circ}{\rm C}$, which likely corresponds to overlapping signatures for the constituent O and A segments. This DSC thermogram also displays features consistent with a high degree of O segment crystallinity, evidenced by a substantial melting endotherm centered around a melting point at $T_{\rm m} = 37~^{\circ}{\rm C}$. The heat of fusion $\Delta H = 34.5~{\rm J/g}$ obtained by endothermic melting peak integration implies a crystalline O weight fraction $X_{\rm c} = \Delta H/(w_{\rm O}\Delta H_0) = 0.72$, where the diblock O weight fraction $w_{\rm O} = 0.24$, and $\Delta H_0 = 200~{\rm J/g}$ is the melting enthalpy for perfectly crystalline O. As compared to the precursor O homopolymer with $T_{\rm m} = 52~^{\circ}{\rm C}$ and $X_{\rm c} = 0.73~{\rm (Figure~S6)}$, the O segment in OA21 displays a similar degree of crystallinity with a severely

depressed $T_{\rm m}$. This may be attributed to the increased degree of chain folding required in the diblock case to match the segmental interfacial area of the semicrystalline O block with that of the substantial amorphous A-block at the diblock junction. 49,64 This melting point depression may be estimated in terms of the Gibbs-Thomson (G-T) effect, which predicts a crystalline domain thickness of 2.4 nm (see the Supporting Information for detailed calculations). The DSC cooling trace in Figure 2 also indicates that deep undercooling is required to recrystallize the O domain of OA21, implying a significant kinetic barrier to O crystallization that may be attributed to the anisotropic arrangement of the O blocks in the melt imposed by the large amorphous A-block (vide infra). We note that no order-to-disorder or order-to-order transitions were observed by DSC, consistent with the fact that microstructural transitions of asymmetric particle-forming diblock copolymer melts typically exhibit transition enthalpies several orders of magnitude less than those associated with segment backbone crystallization $(\Delta H_{\rm ODT} \lesssim 0.1 \text{ J/g}).^6$

Morphologies on Heating OA21. Morphological studies of OA21 relied principally on *in situ* high-resolution, temperature-dependent synchrotron SAXS. The 1D SAXS traces given in Figure 3 indicate that OA21 displays six distinct

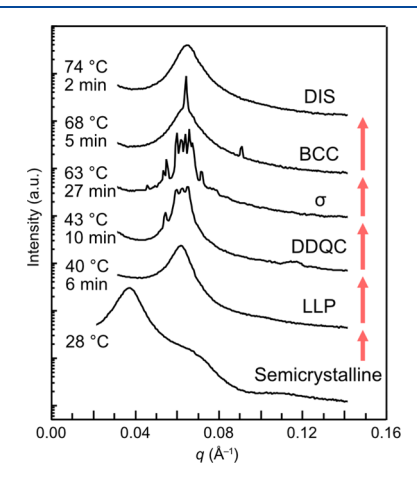


Figure 3. Temperature-dependent SAXS profiles obtained from OA21 on heating. Temperatures at the left of each trace indicate the sample temperature at exposure. Associated time stamps refer to the time elapsed between the previously marked temperature below the trace in question with a ramp rate of 20 °C/min. Phase assignments to the right of each trace refer to a semicrystalline state, a liquid-like packing (LLP) of spheres, a DDQC, a FK σ phase (σ), a BCC packing of spheres, and a fluctuating DIS, respectively, from bottom to top.

states on ramping the temperature from 22 °C through the order-to-disorder transition $T_{\rm ODT}$ = 69 °C over an interval of 50 min. Below $T_{\rm m}$ = 37 °C, SAXS traces consistent with the representative 28 °C scattering profile shown in Figure 3 were recorded. Instead of the sharp Bragg reflections characteristic of a well-ordered microstructure, these patterns instead display a series of broad correlations with sharply diminished intensities at $q > q^*$. Assuming that these correlations correspond to those associated with a poorly ordered crystalline lamellar (L_c) structure, the initial $q^* = 0.037$ Å⁻¹ would correspond to a full period spacing d = 17.1 nm ($d = 2\pi/q^*$). From this value, we deduce that the total O layer thickness is $d_0 = f_0 d = 3.6$ nm and the crystalline O domain thickness is $d_{0,c} = X_c d_0 = 2.6$ nm, where $X_c = 0.75$. Within the monoclinic crystal structure of O homopolymer, each repeat

unit contributes 0.278 nm along the O 3 \times 7/2 helix axis. Accordingly, the O block comprising 45 monomer units has a full contour length of $l_{\rm O}=12.5$ nm, of which $l_{\rm c,O}=9.0$ nm participates in crystallization ($l_{\rm c,O}=X_{\rm c}l_{\rm O}$). In order to fit into the observed 2.6 nm crystalline O domains, the crystalline O blocks must be folded on average 2.5 times, assuming a O block monolayer with a perpendicular O crystal stem orientation relative to the microphase-separated interface, as illustrated in Figure 4A. High degrees of non-integer chain

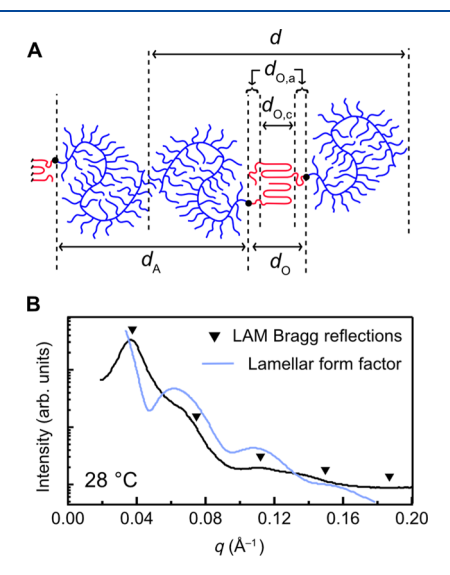


Figure 4. (A) Schematic of the characteristic length scales of the L_c morphology of OA21, including the full period spacing (d), the A domain layer thickness (d_A) , and the PEO domain layer thickness (d_O) . The O domain layer is further decomposed into constituent amorphous $(d_{O,a})$ and crystalline $(d_{O,c})$ regions. Chain conformations shown are idealized, and the details of A-block chain end distributions are unknown. (B) 1D-SAXS trace of sample OA21 in the semicrystalline state observed at ambient temperature.

folding in semicrystalline monolayers with stems perpendicular to the layer interface are anticipated by the diMarzio—Guttman—Hoffman theory and have been observed experimentally during breakout crystallization in compositionally asymmetric CA diblocks. However, the higher order correlations in the SAXS traces of the semicrystalline phase in OA21 are incommensurate with the expected reflections at $2q^*$, $3q^*$, and so forth for a lamellar structure (Figure 4B). These correlations may instead be rationalized using a lamellar form factor of the type

$$I(q) = \frac{4\pi\Delta\rho^2}{d_{\rm A}q^4} [1 - \cos(qd_{\rm A})e^{-q^2\sigma^2/2}]$$
 (1)

where $\Delta \rho$ is the electron density contrast, σ is the layer thickness dispersity, and $d_{\rm A}=13.5~{\rm nm}~[d_{\rm A}=(1-f_{\rm O})d]$ is the amorphous A layer thickness. Using an arbitrary value for $\Delta \rho$ and $\sigma=0.10$ yields a form factor (the solid blue line in Figure 4B) that qualitatively matches the observed SAXS pattern. A Lorentz corrected version of Figure 4B may be found in the Supporting Information, Figure S7. Notably, the crystal thickness $d_{\rm O,c}=2.6~{\rm nm}$ used in this analysis is close to $d_{\rm O,c}=2.4~{\rm nm}$ predicted by the Gibbs—Thomson (G—T) analysis (see Supporting Information eq S10). It is also possible that the semicrystalline state does not consist of layers but is instead characterized by discontinuous O domains by way of

core-confined crystallization from the micellar melt.^{70,71} Accordingly, form factors for other structures including spheres, cylinders, and prolate ellipsoids were compared against the semicrystalline SAXS trace (Figure S8). However, these fits fail to capture the principal scattering features at $q \le 0.10 \text{ Å}^{-1}$.

Raising the temperature of OA21 from 28 to 40 °C over the course of 6 min results in melting of this presumed L_c morphology and formation of an LLP of (nominally spherical) particles. Melting of the crystalline O domain is indicated by an abrupt increase in q^* from 0.037 to 0.062 Å⁻¹ in the SAXS profiles in Figure 3 and disappearance of the sharp Bragg reflections associated with the O crystals in the associated wide-angle X-ray scattering patterns (Figures S9 and S10). The assignment of the LLP state was informed by prior studies of supercooled particle-forming diblock copolymer melts. LLP refers to a metastable DIS far below T_{ODT} , which is characterized by a vanishing concentration of free chains and sharp interdomain interfaces typical of a strongly segregated melt that lacks any crystallographic order in the constituent particle arrangement. 47,72-74 Takagi et al. previously documented the related formation of an LLP state from the L_c phase of a CA diblock on heating,⁴⁸ which subsequently evolved into a BCC packing with time or at elevated temperatures.

Heating the OA21 LLP to 43 °C over the course of 10 min instead leads to the rapid emergence of a cluster of one relatively sharp and three modestly broad Bragg reflections (Figure 5A). Drawing on a body of prior observations of similar 1D-SAXS patterns, ^{26,30} of which some have been accompanied by transmission electron or atomic force

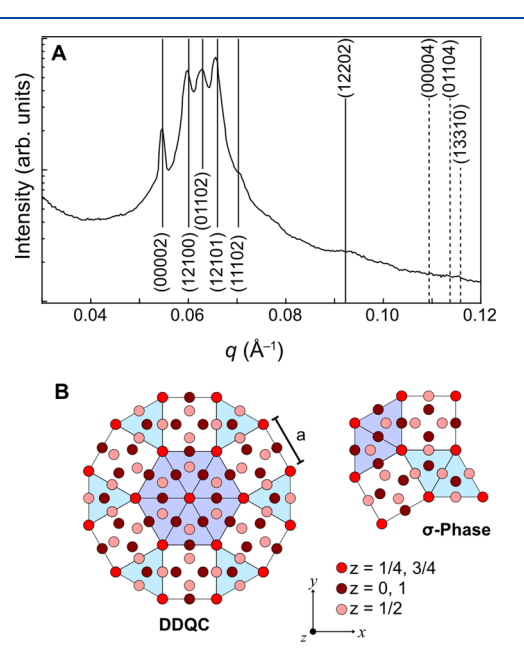


Figure 5. (A) 1D-SAXS intensity profile for the DDQC obtained at 43 °C assigned using the five-dimensional indexing scheme for the expected Bragg reflections with unit cell parameters c=23.0 nm and a=22.6 nm. (B) Schematic depiction of the closely related structural motifs underlying the DDQC and FK σ phase, illustrated using projections along the spatially periodic z-axis (c-direction) of the actual structures as decorated square-triangle tilings with edge length a. The two different triangle types exhibit different out-of-plane spatial arrangements along the c-direction.

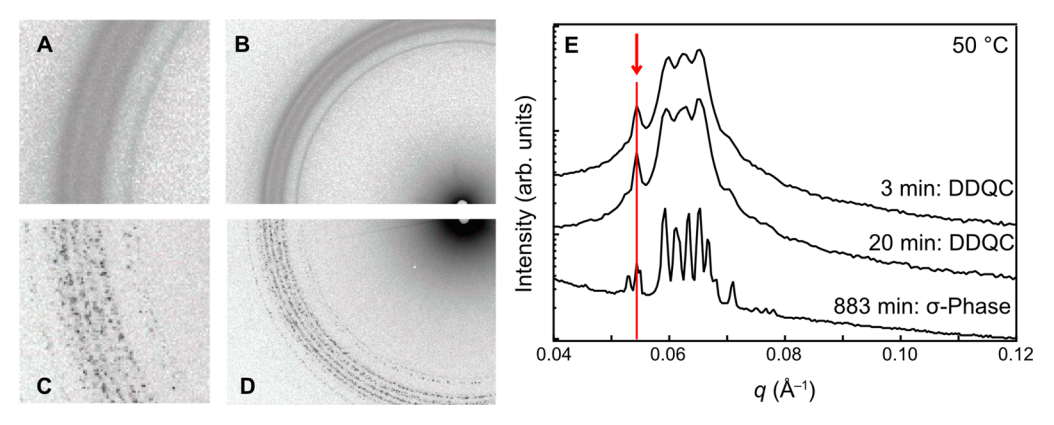


Figure 6. Images of 2D SAXS patterns acquired from OA21 isothermally annealed at 50 °C for 3 min (A and B) and for 883 min (B and D) and the corresponding azimuthally integrated 1D-SAXS intensity profiles that demonstrate the time-dependent evolution of the DDQC into a FK σ phase. The red line in (E) demarcates the (00002) reflection of DDQC, which coincides with the (002) reflection of the σ phase, indicative of a common layer spacing in the two structures.

microscopy images, 6,20,29,75 we assign this structure as a polycrystalline DDQC. This DDQC is an aperiodic 2D structure exhibiting $P12_6/mcm$ symmetry, which comprises periodically stacked layers in which particles are aperiodically arranged with a 12_6 screw axis. Owing to the lack of periodicity of this structure in 3D space, a 5D indexing scheme has been employed for structure assignment following intermetallic structure precedents 32,36 and related reports in soft matter systems. 26,30 On this basis, we calculate that the periodic layer spacing is c=23.0 nm with an in-plane periodicity length scale of a=22.6 nm with a nearly ideal c/a=1.02. Although the DDQC effectively exhibits an infinite unit cell, idealized DDQC structures may be visualized using 2D square-triangle tilings with the uniform edge length a depicted in Figure 5B. 70,77

On further heating to 63 °C over the course of 27 min, the broad Bragg reflections of the DDQC are replaced by a dense cluster of sharp reflections indicative of a periodic FK σ phase with $P4_2/mnm$ symmetry and large tetragonal until cell parameters a=43.4 nm and c=22.9 nm (c/a=0.528). Since the σ phase is a periodic 3D crystalline approximant of a DDQC, one expects the preservation of certain structural elements in this transition. Notably, the periodic layer spacing c=22.9 nm is nearly invariant in this order-to-order transition. Furthermore, the σ phase may also be conceptualized in terms of the related square-triangle tiling shown in Figure 5B. Previous experimental observations of diblock copolymer DDQCs have strongly suggested that this aperiodic structure is metastable and evolves to a periodic σ phase with kinetics that reflect the time scales for intermicellar chain exchange. 6,26

Prior to disordering at $T_{\rm ODT}\approx 69$ °C, OA21 undergoes another phase transition in which the dense forest of peaks of the σ phase is replaced by a single, sharp reflection accompanied by a higher order peak at $\sqrt{2}q^*$ on heating from 63 to 68 °C as shown in Figure 3. This pattern is indicative of a BCC arrangement of particles with a lattice parameter of a=13.8 nm. The formation of the BCC phase prior to disordering upon heating is anticipated in theory and is often experimentally observed, provided concentration fluctuations do not mask the transition. Above $T_{\rm ODT}$, a disordered phase is observed as evidenced by the 74 °C pattern in Figure 3. This disordered phase (DIS) at $T > T_{\rm ODT}$ has a slightly broader q^* peak than that of the low-temperature LLP state, presumably due to weaker segregation between the core

and corona blocks. Motivated by this rich phase behavior exhibited by a single OA21 diblock copolymer, we further explored the nature of the observed phase transitions with specific attention to the conditions required for DDQC formation.

Temporal Stability of DDQC in OA21. Since previous reports indicated that the DDQC is a long-lived metastable state that can evolve into the equilibrium FK σ phase over time, we sought to assess the temporal stability of the OA21 DDQC on isothermal annealing at 50 °C (Figure 6). Prior to SAXS data acquisition, the sample was heated from the semicrystalline state ($T \le 37$ °C) to $T_{\rm anneal} = 50$ °C over the course of 4 min. After 3 min, a DDQC structure developed as evidenced by the 2D SAXS pattern (Figure 6A,B) and the corresponding 1D intensity profile in Figure 6E from which we derived the lattice constants a = 22.7 nm and c = 23.1 nm. The radially symmetric Debye-Scherrer rings in the 2D pattern encode a reciprocal lattice constructed of concentric spheres corresponding to an average of many small, randomly oriented grains in real space consistent with a polycrystalline DDQC. Qualitatively, the pattern does not change over 20 min at 50 °C. However, after 883 min, the four prominent and azimuthally homogeneous Debye-Scherrer rings of the DDQC pattern are replaced by a dense set of azimuthally heterogeneous rings (Figure 6C,D). The resulting 1D intensity profiles derived from these patterns (Figure 6E) unambiguously index to the σ phase with a = 43.9 nm and c = 23.1 nm. We again note the common c value between the DDQC and σ structures, indicated by the coincidence of the (00002) and (002) reflections in the respective SAXS patterns (red line in Figure 6E). These results directly indicate that the OA21 DDQC state is metastable with respect to the σ phase at 50 °C.

Given the invariance in the periodic layer spacings of the DDQC and σ phases, one may be tempted to suggest that only in-plane particle rearrangements are required for the DDQC-to- σ transition. However, the 2D SAXS patterns for the σ phase (Figure 6C,D) indicate widespread grain coarsening through the loss of radial symmetry on account of a smaller number of large grains contributing to the average reciprocal space structure, which leads to a localization of the Bragg reflection intensities in discrete spots. The formation of "spotty" rings even in the σ phase (002) reflection suggests significant changes in the overall grain structure and orientation distribution. Taken together, the 2D SAXS patterns

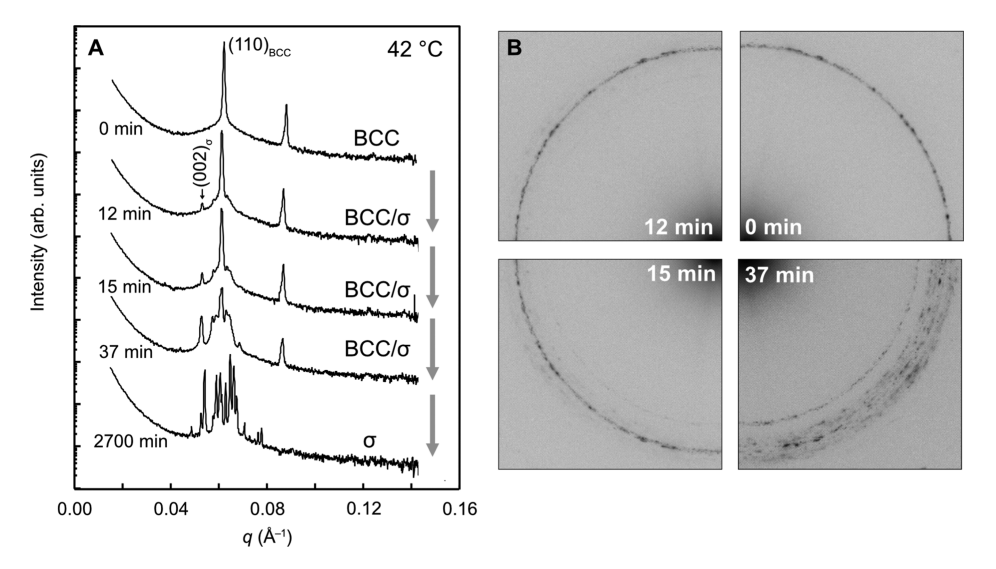


Figure 7. Structural evolution of OA21 following quenching to 42 °C after pre-annealing at 66 °C for 6 min to foster BCC ordering. Time stamps in both A and B correspond to the time elapsed since temperature reached the 42 °C set point. 1D SAXS traces are shown in (A), which correspond to the 2D patterns in (B) following time stamps marking each. 2D patterns are rotated from their original orientation to facilitate direct comparison of the relative positions of each of the rings.

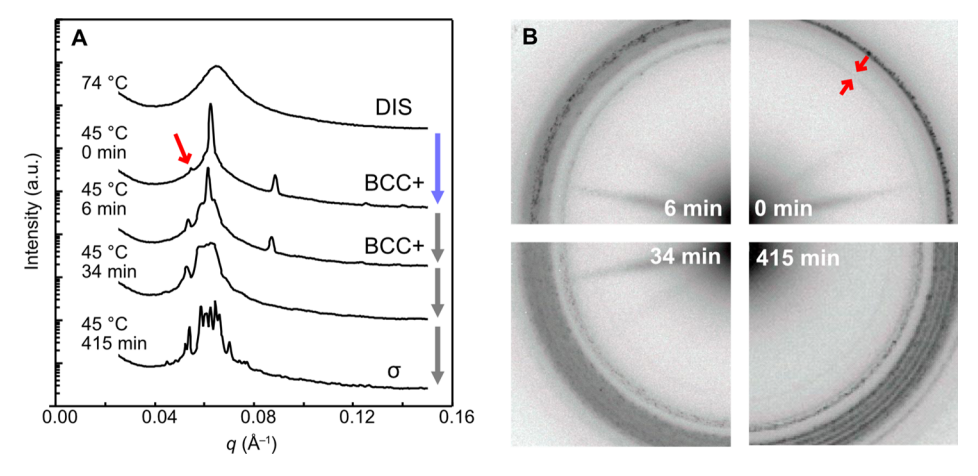


Figure 8. Structural evolution of OA21 following quenching to 45 °C from 74 °C through combined 1D (A) and 2D (B) SAXS patterns. 2D SAXS patterns are rotated from their original orientation to facilitate direct comparison of the relative positions of each of the rings. The red arrows highlight the development of a low-q feature in the initial BCC pattern, which is discussed more in the text.

in Figure 6 indicate that the growth of the σ phase from the metastable DDQC occurs in all crystallographic directions and that purely in-plane particle-based rearrangements do not lead to this transition. Instead, the growth of σ from the DDQC is marked by dominance of a greatly reduced number of large grains.

Conditions for DDQC Formation: Quenches from High 7. Given that the OA21 DDQC readily forms from a low-temperature LLP state derived from melting of the L_c phase, we sought next to understand whether this aperiodically ordered phase could also be accessed on quenching a periodic BCC micelle packing to a temperature characterized by an equilibrium FK σ phase (Figure 7). A well-formed BCC structure was obtained by isothermally annealing OA21 at 66 °C for 6 min. Immediately following sample thermal quenching to 42 °C (t = 0 min), SAXS analyses reveal that the prominent primary (110) and secondary (200) peaks of BCC remained unperturbed with the expected (211) form factor extinction associated with the size of the O particle cores (Figure 7A). The textured nature of the (110) peak in the top

right panel of Figure 7B is indicative of large BCC grains, reflecting the expected nucleation-limited growth of this phase in proximity to $T_{\rm ODT}$ = 69 °C. On quenching to 42 °C, this BCC lattice is metastable and the characteristic layer spacing (002) reflection of the σ phase begins to materialize after 12 min of isothermal annealing. Note that this SAXS peak could also correspond to the (00002) reflection of a DDQC, a possibility not directly refuted by the poorly resolved and lowintensity reflections flanking the BCC (110) peak at t = 12min. At t = 15 min and 37 min, the SAXS patterns exhibit pairs of maxima located on either side of the BCC (110) peak, which are inconsistent with the DDQC scattering signature (cf., Figure 5). From patterns obtained between 12 and 37 min of isothermal annealing at 42 °C (Figure 7B), we observe significant texture in the new SAXS rings indicative of large, ordered grain formation reminiscent of Figure 6C,D, which suggests a direct BCC \rightarrow BCC + $\sigma \rightarrow \sigma$ transition that is complete after 2700 min. Additional 2D SAXS patterns are provided in Figure S11. Note that the spotty rings lead to azimuthally integrated peak intensities that differ from

expectation based on the literature. 11 This transition sequence stands in stark contrast to the previous case, wherein the structurally disorganized (amorphous) LLP rapidly evolves into a polycrystalline DDQC with a slower transition to the σ phase with coarse grain sizes. Considering the structural similarities between the σ phases nucleated from BCC and DDQC and the timescales in their formation (hours), both are likely products of nucleation-directed phase growth, as opposed to the rapid diffusion-limited process of LLP \rightarrow DDQC. Furthermore, the BCC $\rightarrow \sigma$ transition is direct, evidenced by the 37 min pattern of Figure 7A, which demonstrates clear BCC/ σ coexistence as the textured BCC pattern is smoothly replaced with an equally textured σ pattern. Accordingly, we find that an intermediate DDQC phase is not seeded when quenching BCC below the BCC/ σ order–order transition.

Next, we sought to understand whether quenching the DIS state obtained from T = 74 °C > T_{ODT} to 45 °C forms a DDQC by analogy to a processing strategy previously reported by Gillard et al.26 From the SAXS patterns given in Figure 8A,B, we observe very rapid nucleation of a BCC phase with prominent (110) and (200) SAXS peaks at the t = 0 min time point at 45 °C. We surmise that the low barrier to BCC nucleation may originate with the high degree of chain mobility in this system on account of the low T_g 's of the O and A blocks. We avoid any comparative analyses of the grain sizes associated with the BCC phases shown in Figures 7 and 8, as these data were acquired at different synchrotron SAXS beamlines with different beam and detector pixel sizes. Intriguingly, a low-intensity low-q peak within the "skirt" of the primary (110) BCC peak almost immediately appears in the t = 0 min X-ray pattern obtained at 45 °C. This feature is indicated by the red arrows in Figure 8. This peak corresponds to an isotropic Debye-Scherrer ring in the associated 2D SAXS pattern, symptomatic of either the (002) or (00002) layer spacings of the σ or DDQC phases, respectively. At t = 6min post-quench, this isotropic ring becomes more prominent alongside a wider isotropic ring growing in on either side of the originally textured (110) BCC peak. Furthermore, several discrete scattering spots in the (002)/(00002) ring are noted. Additional 2D SAXS patterns corresponding to Figure 8A are provided in Figure S12. After t = 34 min, the BCC phase has all but disappeared and is replaced by a more complex scattering signature that contains distinctive elements of both the high-intensity trio of low q peaks of a DDQC, and the extra peaks and shoulders that arise from discrete spots in the 2D SAXS patterns that are consistent with a σ phase. In contrast to the σ/BCC coexistence noted 37 min after quenching the ordered BCC phase to 42 °C, quenching from disorder yields a DDQC/ σ coexistence with no signs of BCC after 34 min at 45 °C. On the basis of the aforementioned BCC $\rightarrow \sigma$ transition triggered by thermal quenching (Figure 7), we suggest that regions of the sample lacking lattice order post-quench enable transient DDQC formation while the regions of the sample that nucleate BCC directly transition to the σ phase. In other words, the seeds for DDQC formation are sown in the hightemperature and low-temperature LLP states. We do not attribute the features in these SAXS traces to serial BCC \rightarrow DDQC $\rightarrow \sigma$ transitions, and instead assert two parallel pathways are operative that lead to either a BCC or a DDQC packing that transforms to a σ phase.

Crystallization of OA21. A distinguishing feature of this study is the semicrystalline nature of the O block of OA21,

which enables direct access to a pure LLP state on melting the L_c phase, thereby circumventing any microstructural evolution triggered by quenching the thermally disordered state. Furthermore, this sequence of observed phase transitions including DDQC formation is fully repeatable from SAXS traces collected on thermal cycling of OA21 as shown in Figure 9. The traces given in Figure 9A belong to the same heating

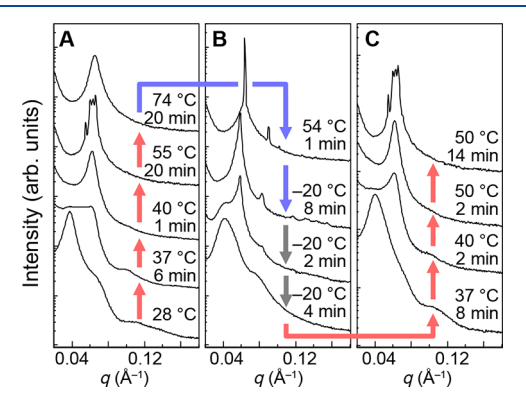


Figure 9. *In situ* temperature-dependent SAXS of OA21 demonstrating that the DDQC structure, the 55 $^{\circ}$ C pattern in (A) and 50 $^{\circ}$ C pattern in (B), may be repeatedly recovered by crystallizing (B) and re-melting (C) the O-segments of the diblock. Time stamps correspond to the time elapsed since the previous temperature following the arrows. Temperature changes were enacted with a heating or cooling rate of 10 $^{\circ}$ C/min.

ramp as Figure 3 and reiterate the formation of the DDQC on melting the L_c state, now with an intermediate pattern inserted at $T=37\,^{\circ}\text{C}$, that was taken 2 min after reaching that temperature. While the real-space structure giving rise to this transient SAXS signature remains obscure, we speculate that it reflects a coexistence of a diminishing L_c phase with concomitant growth of the LLP.

Following melt disordering (shown in Figure 9A), Figure 9B illustrates the processes of recrystallizing the O domain observed by in situ SAXS. The pattern at 54 °C was taken 1 min following a quench from 74 °C and demonstrates the rapid nucleation of BCC with a lattice parameter a = 14.0 nm. Cooling from that point to -20 °C over 5 min followed by isothermal annealing for 9 min gives rise to the first (top) of the three -20 °C patterns, which retain the BCC Bragg diffraction peaks, albeit with an enlarged lattice constant of a =15.2 nm and considerable peak broadening. Since $T_{\rm m}$ = 37 °C, this BCC structure is metastable with respect to L_c. After two additional minutes, a low-q feature materializes at the base of the (110) primary BCC peak (Figure 9B, middle -20 °C trace). This feature increases in intensity over an additional 4 min, during which all signs of BCC structure are destroyed (Figure 9B, bottom -20 °C trace) by O breakout crystallization. Applying the same indexing scheme to this L_c pattern as in Figure 4 reveals a reduced layer periodicity of d =15.2 nm, which corresponds to $d_{\rm O,c}$ = 2.4 nm and three chain folds in the O-monolayer, assuming $X_c = 0.75$.

In Figure 9C, this L_c structure melts into LLP at 40 °C over 3 min and ultimately grows the DDQC, both mirroring the q-spacings observed in Figure 9A and indicating that the L_c may be reversibly formed and melted into a quasicrystal. The high degree of undercooling required to achieve this emulates the results obtained at a faster cooling rate on DSC, implying a

substantial kinetic barrier associated with local chain rearrangements required for $L_{\rm c}$ growth.

Although the *in situ* SAXS experiments employed $T_{\rm c}=-20$ °C, crystallization of OA21 also progresses at higher temperatures, albeit at a considerably slower rate as documented by PLM analyses. PLM reveals that breakout crystallization is macroscopically manifested in the development of spherulites during isothermal crystallization at $T_{\rm c} \geq -10$ °C, evidenced by the distinctive Maltese cross patterns in the optical micrographs presented in Figure 10. The presence

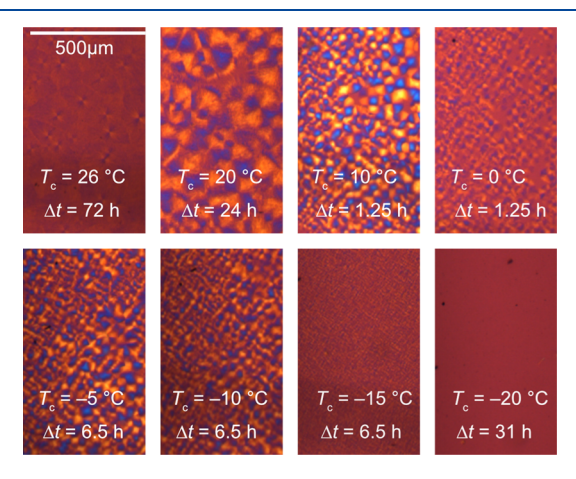


Figure 10. Polarized optical microscopy of sample OA21 after quenching from $T=75~^{\circ}\mathrm{C} > T_{\mathrm{ODT}}$ to various crystallization temperatures (T_{c}) for various periods of time.

of spherulites is consistent with the L_c structure assigned to SAXS patterns. The absence of spherulitic order in the $T_c \leq -15$ °C panels of Figure 10 marks either the absence of longrange order in the L_c structure or the onset of confined crystallization. However, the sudden and complete disruption of the BCC structure in the semicrystalline state in the -20 °C SAXS measurements displayed in Figure 9 indicates that rapid breakout crystallization occurs.

DISCUSSION

Quasiperiodic ordering in OA21 always emerges from micelle packings with a minimal long-range lattice order referred to as LLP. This is consistent with the observation of the first reported diblock DDQC by Gillard et al., which was rationalized to reflect the maturation of local tetrahedral clustering thought to exist in the LLP state.²⁶ However, this rationale was not based on direct real-space imaging of the local LLP structure. The detailed structural characteristics of this state remain elusive, yet are presumed to be related to those of both hard and soft particle glasses. 80-84 Thus, LLP refers to a jammed state of diblock micelles wherein slow intermicellar mass exchange inhibits the system from adjusting the nonequilibrium particle size distribution of this supercooled DIS to one commensurate with a long-range lattice order. 47,72-74 Accordingly, the nucleation of local tetrahedral packing into a metastable DDQC is thought to arise primarily from particle-based rearrangements. This assertion is bolstered by theories of DDQC formation in systems of identical particles governed by pair potentials that exhibit similar combinations of soft corona—corona and hard core—corona repulsions that regulate diblock micelle self-assembly. 85–88

Foundational to this line of thinking is the general tendency for tetrahedral close packing in soft micellar systems.⁸⁹ In diblock copolymers, the spontaneous formation of specific and discrete particle size distributions required by spatially periodic TCP structures such as the σ phase arises from local particle shape optimization subject to interfacial area minimization.³⁹ This embodies a simultaneous minimization of enthalpically costly particle core—corona interfacial tension and entropically costly variations in the extent of diblock chain stretching constrained by melt incompressibility, which precludes the formation of spherical particles. Instead, diblock copolymer particles assume the shape of polyhedral WS cells associated with FK phases such as σ . Recent careful examinations of these geometric principles have established FK σ and A15 phases as equilibrium structures in diblock melts, with σ favored for relatively lower core volume fractions $f_{\rm core} \le 0.25$, as is the case for OA21 and A15 favored for higher core volume fractions approaching and exceeding $f_{\text{core}} \approx$ $0.30^{25,31}$

In contrast, the precise reason for the experimental observation of metastable DDQCs prior to equilibrium approximant phases such as σ or A15 remains obscure. Also, occurrence of the C14 and C15 Laves phases in diblock copolymers following quenching of the disordered melt in liquid nitrogen and subsequent heating to $T < T_{\rm ODT}$ is not understood. Neither C14 or C15 is predicted to be an equilibrium state of order in single-component diblock copolymers. However, the phase transitions exhibited by OA21 under a variety of thermal processing routes, outlined in Figure 11, offer some clues concerning the appearance of the DDQC.

Central to this investigation is the formation of an LLP state upon melting of L_c , which bypasses the nucleation of any higher temperature structures. Exactly how L_c transitions to LLP is unknown; however, we speculate that local clusters of diblocks within the melted layers coalesce and pinch off in order to minimize O–A contacts at temperatures well below

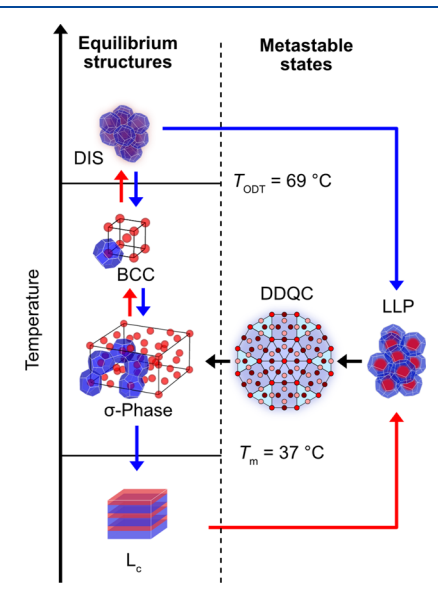


Figure 11. Schematic of morphological transitions observed for the OA21 diblock. Red arrows denote heating, blue arrows cooling, and black arrows isothermal annealing. Experimentally observed phase coexistences due to experimental heat transfer limitations were omitted for simplicity.

the $T_{\rm ODT}$, where the free diblock concentration nominally vanishes. Spontaneous layer fission likely results in a heterogeneous, non-equilibrium particle size distribution. Over the course of minutes, these particles adopt a polycrystalline DDQC structure, which, on heating or on isothermal annealing, gives way to the σ phase with large grain sizes. The rapidity of DDQC formation implies a formation pathway based primarily on local particle rearrangements, in contrast to the comparatively longer timescale associated with σ formation. We posit that the latter slow process requires ratelimiting chain exchange between particles to adjust their sizes and shapes. This assertion is consistent with the notion that chain exchange slows as $\exp(-\chi N)$ and thus is very slow well below the T_{ODT} where both DDQC and σ are observed. Particle-based rearrangements that give rise to a DDQC from the LLP are conversely mediated mainly by A matrix chain dynamics, which are fast given that $T_{\rm g,OA21} \approx -70$ °C.

The DDQC $\rightarrow \sigma$ transition is not marked by a significant change in the characteristic length scales of the system, a principle demonstrated by the shared layer spacing of both structures through this transition under isothermal conditions (Figure 5). On this basis, we propose that the average particle aggregation number ($\langle N_{\rm agg} \rangle$ = 64) remains constant as σ overtakes DDQC with time. Crucially, $\langle N_{\rm agg} \rangle$ discussed in terms of TCP structures represents the mean value of a discrete particle size distribution uniquely defined for each FK phase. However, the size distribution in the aperiodic DDOC is likely broader. In the decorated square-triangle tiling formalism (Figure 5B), the σ phase comprises purely $3^2.4.3.4$ vertices, where three triangles (3) and two squares (4) encircle each vertex wherein degeneracy is conveyed through the superscript.⁹¹ Quasiperiodic Stampfli tilings giving rise to DDQCs, on the other hand, follow a dodecahedral motif of a central 3^6 vertex encircled by six σ -type 3^2 .4.3.4 vertices, supplemented by regions of local 33.42 vertices. 76,77 This variability in local packing constraints is accompanied by an expansive set of particle sizes contributing to $\langle N_{
m agg} \rangle$. Therefore, we infer that changes in $N_{\rm agg}$ during DDQC $\rightarrow \sigma$ are confined not only to the absolute value of $\langle N_{\rm agg} \rangle$ but the shape and breadth of the underlying N_{agg} distribution. Accordingly, the more diverse sets of particle types packing into the myriad of local structures comprising the DDQC more closely mimics the heterogeneity present in the LLP state than that of the σ phase. Therefore, the formation of DDQC out of the supercooled LLP state may represent a temporary compromise that optimizes local particle shape for a system with broader, non-equilibrium particle size distribution.

Further support for this argument may be found in the thermal transitions on cooling. Figure 11 suggests that a DDQC forms on quenching from DIS to LLP but not from BCC to σ . The latter claim is supported by the fact that both supercooled BCC states studied here, reached via quenching equilibrium BCC (Figure 7) or DIS states (Figure 8) to 42 or 45 °C, respectively, transformed directly into well-ordered σ phases via BCC/ σ coexistence. Although the nucleation of BCC during the DIS \rightarrow 45 °C quench obfuscates unequivocal observation of the DIS → LLP → DDQC progression, the DDQC characteristic of SAXS patterns acquired in this experiment suggest the presence of increased disorder during this experiment relative to the BCC \rightarrow 42 $^{\circ}$ C quench. Taken together, these observations underscore that DDQC formation sensitively depends on the immediately preceding state. The BCC lattice, which has a narrow particle size distribution on

account of its single coordination environment, provides a favorable metastable platform from which σ can develop directly via the same intermicellar mass exchange mechanism at work in the DDQC $\rightarrow \sigma$ transition. This raises the question as to why these BCC particles do not rearrange into a DDQC, as with the LLP state. We posit that the shape and breadth of the particle size distribution underlying each of these phases modulates the observed metastable states, wherein the intermediate state does not possess a broader particle size dispersity than either the initial or final state. Both the LLP \rightarrow DDQC $\rightarrow \sigma$ and BCC $\rightarrow \sigma$ progressions present monotonic trends in the underlying particle size heterogeneity, which correspond to kinetically favorable mass redistribution pathways. This tendency for the metastable intermediate state to closely mirror the properties of the initial state follows the empirical trend put forth by Ostwald in 1897, rationalizing the formation of complex intermediates from a liquid as found by Kim et al.⁴⁷

The LLP state has been established as a vital ingredient to the subsequent formation of a DDQC throughout the diblock literature, irrespective of whether the supercooled LLP state originated from deep thermal quenches, 26 direct liquefaction of freeze-dried powder, 20,31 or melting of a semicrystalline state, including a blend of a CA diblock and a homopolymer. 92 No diblock DDQC has been observed to nucleate on cooling a high-symmetry phase such as BCC, as these thermal pathways only lead directly to σ . 26,92 These observations further establish that the DDQC is a metastable intermediate between LLP and periodic DDQC approximants and that the formation of the DDQC is inextricably linked to the dynamical processes underlying order—order transitions in diblock copolymer melts.

This raises the question of metastability of the diblock copolymer DDQC in the context of the appearance of DDQCs in other soft systems, namely, dendrons $^{30,93-95}$ and dendron-like giant molecules. 18,96 In both cases, the DDQC appears from a disordered LLP state in the phase space vicinity of the A15 and σ approximant phases. Intriguingly, some of these dendron-based DDQC structures form directly on cooling from disorder, 97 and some are remarkably thermally stable, making it difficult to draw conclusions concerning their metastability. 18 Generally, these other systems are characterized by significantly smaller particle aggregation numbers, which may frustrate the formation of the five discrete particle volumes associated with the σ phase, thus favoring the DDQC. Alternatively, restricted mass exchange could present kinetic barriers to the development of the periodic σ structure.

CA diblocks such as the OA system studied here offer the enticing capability to disorder the diblock melt not only on heating but also on cooling, which then affords an additional mechanism for guiding particle size dispersity and thus the symmetry selection pathways of the system. This approach may offer a new route for accessing as yet unobserved metastable FK phases by analogy to recent discoveries of C14 and C15 structures in diblocks. The current study elicits the question of why metastable DDQCs so frequently precede the well-developed σ phase. While many other periodic FK approximants that exhibit different particle size and shape distributions than the σ phase are known, 98 only the C14, C15, A15, and Z phase have been observed in soft matter. Further work mapping this rich free energy landscape of polymer micelle packings will be required to fully resolve this issue.

CONCLUSIONS

The phase transitions of a highly conformationally and compositionally asymmetric OA21 diblock copolymer were investigated via in situ temperature-dependent synchrotron SAXS. Below the melting temperature of the O block, $T_{\rm m} \approx 37$ °C, we found that this system forms a highly asymmetric, layered L_c structure. On melting, rapid layer fission results in the formation of soft glassy LLP of particles that quickly rearrange into a DDQC. With time or temperature, this DDQC evolves into the σ phase that transitions through BCC prior to melt disordering at $T_{\rm ODT}$ = 69 °C on heating. Although the DDQC could be recovered by a rapid quench from $T > T_{ODT}$ to 45 °C, surprisingly, no DDQC was observed on similarly quenching a well-formed BCC lattice. This finding was rationalized in terms of the shape and breadth of the underlying particle size distribution. We speculate that the formation of a DDQC requires a certain breadth in the particle size distribution or aggregation number dispersity. In other words, the unimodal particle distribution characteristic of a well-ordered BCC phase does not spontaneously broaden to favor an aperiodic DDQC tiling but instead smoothly adjusts to the five distinct particle shapes found in the FK σ -phase.

The discovery of a non-poly(lactide)-based DDQC/ σ -forming diblock highlights the independence of TCP structure formation on the chemical nature of the self-assembling polymer building blocks, suggesting the importance of widely applicable, fundamental geometric principles. Whether or not the relationship between the still mysterious LLP state and the subsequent DDQC, formed *en route* to an equilibrium σ phase, may be applied to the broader range of mesoscopic systems displaying analogous behavior, spanning sub 10 nm structures composed of wedge-shaped dendrons to 100 nm unit cells of tetrablock terpolymers, remains an open question.

Perhaps most intriguing are the possibilities afforded by the semicrystalline nature of the O block of OA21. In the present study, this was used to repeatedly form a DDQC from a pure LLP state without traversing the high-temperature regions of the phase space. We anticipate that similar CA diblocks will find use in accessing new diblock copolymer melt morphologies through non-classical routes.

ASSOCIATED CONTENT

Supporting Information

The Supporting Information is available free of charge at https://pubs.acs.org/doi/10.1021/acs.macromol.0c02871.

Experimental details and additional characterization data $\left(\text{PDF} \right)$

AUTHOR INFORMATION

Corresponding Authors

Mahesh K. Mahanthappa — Department of Chemical Engineering and Materials Science, University of Minnesota, Minneapolis, Minnesota 55455, United States; oorcid.org/ 0000-0002-9871-804X; Email: maheshkm@umn.edu

Frank S. Bates — Department of Chemical Engineering and Materials Science, University of Minnesota, Minneapolis, Minnesota 55455, United States; orcid.org/0000-0003-3977-1278; Email: bates001@umn.edu

Authors

Andreas J. Mueller – Department of Chemical Engineering and Materials Science, University of Minnesota, Minneapolis, Minnesota 55455, United States

Aaron P. Lindsay – Department of Chemical Engineering and Materials Science, University of Minnesota, Minneapolis, Minnesota 55455, United States; orcid.org/0000-0003-0223-193X

Ashish Jayaraman — Department of Chemical Engineering and Materials Science, University of Minnesota, Minneapolis, Minnesota 55455, United States; orcid.org/0000-0001-7071-7419

Timothy P. Lodge — Department of Chemical Engineering and Materials Science and Department of Chemistry, University of Minnesota, Minneapolis, Minnesota 55455, United States; orcid.org/0000-0001-5916-8834

Complete contact information is available at: https://pubs.acs.org/10.1021/acs.macromol.0c02871

Notes

The authors declare no competing financial interest.

ACKNOWLEDGMENTS

Financial support for this work was provided by National Science Foundation grants DMR-1801993 (A.J.M., A.P.L., and F.S.B.) and CHE-1807330 (A.J. and M.K.M.) and a National Science Foundation Graduate Research Fellowship under grant no. 00039202 (A.P.L.). SAXS experiments were carried out at Sector 12 and Sector 5 of the Advanced Photon Source (APS). The Sector 5 DuPont-Northwestern-Dow Collaborative Access Team (DND-CAT) was supported by E.I. DuPont de Nemours & Co., the Dow Chemical Company, and Northwestern University. Use of the APS, an Office of Science User Facility operated for the U.S. Department of Energy (DOE) Office of Science by Argonne National Laboratory, was supported by the U.S. DOE under contract no. DE-AC02-06CH11357. Parts of this work, including lab source SAXS analyses, were carried out in the Characterization Facility at the University of Minnesota, which receives partial support from NSF through the UMN MRSEC (DMR-1420013 and DMR-2011401). ¹H NMR spectra used in this study were collected on a Bruker Avance II HD 400 MHz spectrometer purchased by the Office of the Vice President of Research, the College of Science of and Engineering, and the Department of Chemistry at the University of Minnesota. MALDI-ToF data were obtained at the Mass Spectroscopy Laboratory located in the Chemistry Department at the University of Minnesota, supported by the Office of the Vice President of Research, the College of Science and Engineering, and the Department of Chemistry at the University of Minnesota, as well as The National Science Foundation (NSF, award CHE-1336940).

REFERENCES

- (1) Su, Z.; Zhang, R.; Yan, X. Y.; Guo, Q. Y.; Huang, J.; Shan, W.; Liu, Y.; Liu, T.; Huang, M.; Cheng, S. Z. D. The Role of Architectural Engineering in Macromolecular Self-Assemblies via Non-Covalent Interactions: A Molecular LEGO Approach. *Prog. Polym. Sci.* **2020**, *103*, 101230.
- (2) Vargas, R.; Mariani, P.; Gulik, A.; Luzzati, V. Cubic phases of lipid-containing systems: The structure of phase Q²²³ (Space group Pm3n). An X-ray scattering study. *J. Mol. Biol.* **1992**, 225, 137–145.

- (3) Kim, S. A.; Jeong, K.-J.; Yethiraj, A.; Mahanthappa, M. K. Low-Symmetry Sphere Packings of Simple Surfactant Micelles Induced by Ionic Sphericity. *Proc. Natl. Acad. Sci. U.S.A.* **2017**, *114*, 4072–4077.
- (4) Shearman, G. C.; Tyler, A. I. I.; Brooks, N. J.; Templer, R. H.; Ces, O.; Law, R. V.; Seddon, J. M. Ordered Micellar and Inverse Micellar Lyotropic Phases. *Liq. Cryst.* **2010**, *37*, 679–694.
- (5) Takagi, H.; Hashimoto, R.; Igarashi, N.; Kishimoto, S.; Yamamoto, K. Frank–Kasper σ Phase in Polybutadiene-Poly(ε -Caprolactone) Diblock Copolymer/Polybutadiene Blends. *J. Phys.: Condens. Matter* **2017**, 29, 204002.
- (6) Lindsay, A. P.; Lewis, R. M.; Lee, B.; Peterson, A. J.; Lodge, T. P.; Bates, F. S. A15, σ , and a Quasicrystal: Access to Complex Particle Packings via Bidisperse Diblock Copolymer Blends. *ACS Macro Lett.* **2020**, *9*, 197–203.
- (7) Mueller, A. J.; Lindsay, A. P.; Jayaraman, A.; Lodge, T. P.; Mahanthappa, M. K.; Bates, F. S. Emergence of a C15 Laves Phase in Diblock Polymer/Homopolymer Blends. *ACS Macro Lett.* **2020**, *9*, 576–582.
- (8) Xie, S.; Lindsay, A. P.; Bates, F. S.; Lodge, T. P. Formation of a C15 Laves Phase with a Giant Unit Cell in Salt-Doped A/B/AB Ternary Polymer Blends. *ACS Nano* **2020**, *14*, 13754–13764.
- (9) Frank, F. C.; Kasper, J. S. Complex Alloy Structures Regarded as Sphere Packings. I. Definitions and Basic Principles. *Acta Crystallogr.* **1958**, *11*, 184–190.
- (10) Frank, F. C.; Kasper, J. S. Complex Alloy Structures Regarded as Sphere Packings. II. Analysis and Classification of Representative Structures. *Acta Crystallogr.* **1959**, *12*, 483–499.
- (11) Lee, S.; Bluemle, M. J.; Bates, F. S. Discovery of a Frank-Kasper Phase in Sphere-Forming Block Copolymer Melts. *Science* **2010**, *330*, 349–353
- (12) Luzzati, V.; Vargas, R.; Gulik, A.; Mariani, P.; Seddon, J. M.; Rivas, E. Lipid Polymorphism: A Correction. The Structure of the Cubic Phase of Extinction Symbol Fd–Consists of Two Types of Disjointed Reverse Micelles Embedded in a Three-Dimensional Hydrocarbon Matrix. *Biochemistry* 1992, 31, 279–285.
- (13) Seddon, J. M.; Zeb, N.; Templer, R. H.; McElhaney, R. N.; Mannock, D. A. An *Fd3m*-Lyotropic Cubic Phase in a Binary Glycolipid/Water System. *Langmuir* **1996**, *12*, 5250–5253.
- (14) Ungar, G.; Liu, Y.; Zeng, X.; Percec, V.; Cho, W. D. Giant Supramolecular Liquid Crystal Lattice. *Science* **2003**, 299, 1208–1211.
- (15) Zeng, X.; Ungar, G.; Liu, Y.; Percec, V.; Dulcey, A. E.; Hobbs, J. K. Supramolecular Dendritic Liquid Quasicrystals. *Nature* **2004**, *428*, 157–160.
- (16) Percec, V.; Peterca, M.; Tsuda, Y.; Rosen, B. M.; Uchida, S.; Imam, M. R.; Ungar, G.; Heiney, P. A. Elucidating the Structure of the Pm3n Cubic Phase of Supramolecular Dendrimers through the Modification of Their Aliphatic to Aromatic Volume Ratio. *Chem.—Eur. J.* **2009**, *15*, 8994–9004.
- (17) Huang, M.; Hsu, C.-H.; Wang, J.; Mei, S.; Dong, X.; Li, Y.; Li, M.; Liu, H.; Zhang, W.; Aida, T.; et al. Selective Assemblies of Giant Tetrahedra via Precisely Controlled Positional Interactions. *Science* **2015**, 348, 424–428.
- (18) Yue, K.; Huang, M.; Marson, R. L.; He, J.; Huang, J.; Zhou, Z.; Wang, J.; Liu, C.; Yan, X.; Wu, K.; et al. Geometry Induced Sequence of Nanoscale Frank-Kasper and Quasicrystal Mesophases in Giant Surfactants. *Proc. Natl. Acad. Sci. U.S.A.* **2016**, *113*, 14195–14200.
- (19) Su, Z.; Hsu, C.-H.; Gong, Z.; Feng, X.; Huang, J.; Zhang, R.; Wang, Y.; Mao, J.; Wesdemiotis, C.; Li, T.; et al. Identification of a Frank-Kasper Z phase from shape amphiphile self-assembly. *Nat. Chem.* **2019**, *11*, 899–905.
- (20) Chanpuriya, S.; Kim, K.; Zhang, J.; Lee, S.; Arora, A.; Dorfman, K. D.; Delaney, K. T.; Fredrickson, G. H.; Bates, F. S. Cornucopia of Nanoscale Ordered Phases in Sphere-Forming Tetrablock Terpolymers. ACS Nano 2016, 10, 4961–4972.
- (21) Bates, F. S.; Fredrickson, G. H. Block Copolymers-Designer Soft Materials. *Phys. Today* **1999**, *52*, 32–38.
- (22) Bates, F. S.; Fredrickson, G. H. Conformational Asymmetry and Polymer-Polymer Thermodynamics. *Macromolecules* **1994**, 27, 1065–1067.

- (23) Xie, N.; Li, W.; Qiu, F.; Shi, A. C. σ Phase Formed in Conformationally Asymmetric AB-Type Block Copolymers. *ACS Macro Lett.* **2014**, *3*, 909–910.
- (24) Schulze, M. W.; Lewis, R. M.; Lettow, J. H.; Hickey, R. J.; Gillard, T. M.; Hillmyer, M. A.; Bates, F. S. Conformational Asymmetry and Quasicrystal Approximants in Linear Diblock Copolymers. *Phys. Rev. Lett.* **2017**, *118*, 207801.
- (25) Bates, M. W.; Lequieu, J.; Barbon, S. M.; Lewis, R. M.; Delaney, K. T.; Anastasaki, A.; Hawker, C. J.; Fredrickson, G. H.; Bates, C. M. Stability of the A15 Phase in Diblock Copolymer Melts. *Proc. Natl. Acad. Sci. U.S.A.* **2019**, *116*, 13194–13199.
- (26) Gillard, T. M.; Lee, S.; Bates, F. S. Dodecagonal Quasicrystal-line Order in a Diblock Copolymer Melt. *Proc. Natl. Acad. Sci. U.S.A.* **2016**, *113*, 5167–5172.
- (27) Hayashida, K.; Dotera, T.; Takano, A.; Matsushita, Y. Polymeric Quasicrystal: Mesoscopic Quasicrystalline Tiling in ABC Star Polymers. *Phys. Rev. Lett.* **2007**, *98*, 195502.
- (28) Fischer, S.; Exner, A.; Zielske, K.; Perlich, J.; Deloudi, S.; Steurer, W.; Lindner, P.; Förster, S. Colloidal Quasicrystals with 12-Fold and 18-Fold Diffraction Symmetry. *Proc. Natl. Acad. Sci. U.S.A.* **2011**, *108*, 1810–1814.
- (29) Zhang, J.; Bates, F. S. Dodecagonal Quasicrystalline Morphology in a Poly(styrene-b-isoprene-b-styrene-b-ethylene oxide) Tetrablock Terpolymer. *J. Am. Chem. Soc.* **2012**, *134*, 7636–7639.
- (30) Zeng, X.; Ungar, G.; Liu, Y.; Percec, V.; Dulcey, A. E.; Hobbs, J. K. Supramolecular Dendritic Liquid Quasicrystals. *Nature* **2004**, *428*, 157–160.
- (31) Chang, A. B.; Bates, F. S. Impact of Architectural Asymmetry on Frank-Kasper Phase Formation in Block Polymer Melts. *ACS Nano* **2020**, *14*, 11463–11472.
- (32) Yamamoto, A. Crystallography of Quasiperiodic Crystals. Acta Crystallogr., Sect. A: Found. Crystallogr. 1996, 52, 509–560.
- (33) Levine, D.; Steinhardt, P. J. Quasicrystals: A New Class of Ordered Structures. *Phys. Rev. Lett.* **1984**, *53*, 2477–2480.
- (34) Goldman, A. I.; Kelton, R. F. Quasicrystals and Crystalline Approximants. *Rev. Mod. Phys.* **1993**, *65*, 213–230.
- (35) Iwami, S.; Ishimasa, T. Dodecagonal Quasicrystal in Mn-Based Quaternary Alloys Containing Cr, Ni and Si. *Philos. Mag. Lett.* **2015**, 95, 229–236.
- (36) Ishimasa, T.; Iwami, S.; Sakaguchi, N.; Oota, R.; Mihalkovič, M. Phason space analysis and structure modelling of 100 Å-scale dodecagonal quasicrystal in Mn-based alloy. *Philos. Mag.* **2015**, 95, 3745–3767.
- (37) Niizeki, N.; Mitani, H. Two-Dimensional Dodecagonal Quasilattices. J. Phys. A: Math. Gen. 1987, 20, L405–L410.
- (38) Franz, G. Quasicrystal Structures from the Crystallographic Viewpoint. Ph.D. Dissertation, Swiss Federal Institute of Technology Zürich, Zürich, CH, 1988.
- (39) Reddy, A.; Buckley, M. B.; Arora, A.; Bates, F. S.; Dorfman, K. D.; Grason, G. M. Stable Frank-Kasper Phases of Self-Assembled, Soft Matter Spheres. *Proc. Natl. Acad. Sci. U.S.A.* **2018**, *115*, 10233–10238.
- (40) Lee, S.; Leighton, C.; Bates, F. S. Sphericity and symmetry breaking in the formation of Frank-Kasper phases from one component materials. *Proc. Natl. Acad. Sci. U.S.A.* **2014**, *111*, 17723–17731.
- (41) Kim, K.; Schulze, M. W.; Arora, A.; Lewis, R. M.; Hillmyer, M. A.; Dorfman, K. D.; Bates, F. S. Thermal Processing of Diblock Copolymer Melts Mimics Metallurgy. *Science* **2017**, *356*, 520–523.
- (42) Thomas, E. L.; Kinning, D. J.; Alward, D. B.; Henkee, C. S. Ordered Packing Arrangements of Spherical Micelles of Diblock Copolymers in Two and Three Dimensions. *Macromolecules* **1987**, 20, 2934–2939.
- (43) Ziherl, P.; Kamien, R. D. Maximizing Entropy by Minimizing Area: Towards a New Principle of Self-Organization. *J. Phys. Chem. B* **2001**, *105*, 10147–10158.
- (44) Grason, G. The Packing of Soft Materials: Molecular Asymmetry, Geometric Frustration and Optimal Lattices in Block Copolymer Melts. *Phys. Rep.* **2006**, 433, 1–64.

- (45) Grason, G. M.; DiDonna, B. A.; Kamien, R. D. Geometric Theory of Diblock Copolymer Phases. *Phys. Rev. Lett.* **2003**, *91*, 058304.
- (46) Rappolt, M.; Cacho-Nerin, F.; Morello, C.; Yaghmur, A. How the Chain Configuration Governs the Packing of Inverted Micelles in the Cubic Fd3m-Phase. *Soft Matter* **2013**, *9*, 6291–6300.
- (47) Kim, K.; Arora, A.; Lewis, R. M.; Liu, M.; Li, W.; Shi, A.-C.; Dorfman, K. D.; Bates, F. S. Origins of Low-Symmetry Phases in Asymmetric Diblock Copolymer Melts. *Proc. Natl. Acad. Sci. U.S.A.* **2018**, *115*, 847–854.
- (48) Takagi, H.; Sugino, Y.; Hara, S.; Yamamoto, K.; Shimada, S. Non-Equilibrium Disordered Micelles Observed after Melting of Crystalline-Amorphous Alternating Lamellar Structure in Crystalline-Amorphous Block Copolymers Forming Spherical Morphology. *Colloid Polym. Sci.* **2016**, 294, 993—999.
- (49) DiMarzio, E. A.; Guttman, C. M.; Hoffman, J. D. Calculation of Lamellar Thickness in a Diblock Copolymer, One of Whose Components Is Crystalline. *Macromolecules* **1980**, *13*, 1194–1198.
- (50) Loo, Y.-L.; Register, R. A.; Ryan, A. J. Modes of Crystallization in Block Copolymer Microdomains: Breakout, Templated, and Confined. *Macromolecules* **2002**, *35*, 2365–2374.
- (51) Nandan, B.; Hsu, J. Y.; Chen, H. L. Crystallization Behavior of Crystalline-Amorphous Diblock Copolymers Consisting of a Rubbery Amorphous Block. *Polym. Rev.* **2006**, *46*, 143–172.
- (52) He, W.-N.; Xu, J.-T. Crystallization Assisted Self-Assembly of Semicrystalline Block Copolymers. *Prog. Polym. Sci.* **2012**, 37, 1350–1400
- (53) Jayaraman, A.; Zhang, D. Y.; Dewing, B. L.; Mahanthappa, M. K. Path-Dependent Preparation of Complex Micelle Packings of a Hydrated Diblock Oligomer. *ACS Cent. Sci.* **2019**, *5*, 619–628.
- (54) Ostwald, W. Studien Über Die Bildung Und Umwandlung Fester Körper. 1. Abhandlung: Übersättigung Und Überkaltung. Z. Phys. Chem. 1897, 22, 289–330.
- (55) Van Santen, R. A. The Ostwald Step Rule. J. Phys. Chem. 1984, 88, 5768-5769.
- (56) Armarego, W. L. F.; Chai, C. L. L. Purification of Laboratory Chemicals; Butterworth-Heinemann: Waltham, MA, 2009.
- (57) Houillot, L.; Bui, C.; Save, M.; Charleux, B.; Farcet, C.; Moire, C.; Raust, J.-A.; Rodriguez, I. Synthesis of Well-Defined Polyacrylate Particle Dispersions in Organic Medium Using Simultaneous RAFT Polymerization and Self-Assembly of Block Copolymers. A Strong Influence of the Selected Thiocarbonylthio Chain Transfer Agent. *Macromolecules* **2007**, *40*, 6500–6509.
- (58) Fetters, L. J.; Lohse, D. J.; Richter, D.; Witten, T. A.; Zirkel, A. Connection between Polymer Molecular Weight, Density, Chain Dimensions, and Melt Viscoelastic Properties. *Macromolecules* **1994**, 27, 4639–4647.
- (59) Tong, J. D.; Leclère, P.; Doneux, C.; Brédas, J. L.; Lazzaroni, R.; Jérôme, R. Synthesis and bulk properties of poly(methyl methacrylate)-b-poly(isooctyl acrylate)-b-poly(methyl methacrylate). *Polymer* **2000**, *41*, 4617–4624.
- (60) Wang, J. S.; Matyjaszewski, K. Controlled/"Living" Radical Polymerization. Halogen Atom Transfer Radical Polymerization Promoted by a Cu(I)/Cu(II) Redox Process. *Macromolecules* **1995**, 28, 7901–7910.
- (61) Jankova, K.; Chen, X.; Kops, J.; Batsberg, W. Synthesis of Amphiphilic PS-b-PEG-b-PS by Atom Transfer Radical Polymerization. *Macromolecules* **1998**, *31*, 538–541.
- (62) Hiemenz, P. C.; Lodge, T. P. Polymer Chemistry, 2nd ed.; Taylor & Francis Group: Boca Raton, FL, 2007.
- (63) Matsen, M. W. Polydispersity-Induced Macrophase Separation in Diblock Copolymer Melts. *Phys. Rev. Lett.* **2007**, *99*, 148304.
- (64) Lee, L.-B. W.; Register, R. A. Equilibrium Control of Crystal Thickness and Melting Point Through Block Copolymerization. *Macromolecules* **2004**, *37*, 7278–7284.
- (65) Lee, S.; Gillard, T. M.; Bates, F. S. Fluctuations, Order, and Disorder in Short Diblock Copolymers. *AIChE J.* **2013**, *59*, 3502–3513.

- (66) Takahashi, Y.; Tadokoro, H. Structural Studies of Polyethers, (-(CH₂)_m-O-)_n. X. Crystal Structure of Poly(ethylene oxide). *Macromolecules* **1973**, *6*, 672–675.
- (67) Lotz, B.; Kovacs, A. J. Propriétés des copolymères biséquencés polyoxyéthylène-polystyrène. *Kolloid Z. Z. Polym.* **1966**, 209, 97–114.
- (68) Lotz, B.; Kovacs, A. J.; Bassett, G. A.; Keller, A. Properties of copolymers composed of one poly-ethylene-oxide and one polystyrene block. *Kolloid Z. Z. Polym.* **1966**, 209, 115–128.
- (69) Hong, S.; Yang, L.; MacKnight, W. J.; Gido, S. P. Morphology of a Crystalline/Amorphous Diblock Copolymer: Poly((ethylene oxide)-b-butadiene). *Macromolecules* **2001**, *34*, 7009–7016.
- (70) Huang, Y.-Y.; Chen, H.-L.; Li, H.-C.; Lin, T.-L.; Lin, J. S. Coalescence of Crystalline Microdomains Driven by Postannealing in a Block Copolymer Blend. *Macromolecules* **2003**, *36*, 282–285.
- (71) Huang, Y.-Y.; Yang, C. H.; Chen, H.-L.; Chiu, F.-C.; Lin, T.-L.; Liou, W. Crystallization-Induced Microdomain Coalescence in Sphere-Forming Crystalline—Amorphous Diblock Copolymer Systems: Neat Diblock versus the Corresponding Blends. *Macromolecules* **2004**, *37*, 486–493.
- (72) Dormidontova, E. E.; Lodge, T. P. The Order–Disorder Transition and the Disordered Micelle Regime in Sphere-Forming Block Copolymer Melts. *Macromolecules* **2001**, *34*, 9143–9155.
- (73) Wang, J.; Wang, Z.-G.; Yang, Y. Nature of Disordered Micelles in Sphere-Forming Block Copolymer Melts. *Macromolecules* **2005**, 38, 1979–1988.
- (74) Wang, X.; Dormidontova, E. E.; Lodge, T. P. The Order–Disorder Transition and the Disordered Micelle Regime for Poly(ethylenepropylene-b-dimethylsiloxane) Spheres. *Macromolecules* **2002**, *35*, 9687–9697.
- (75) Shevchenko, E. V.; Talapin, D. V.; Kotov, N. A.; O'Brien, S.; Murray, C. B. Structural Diversity in Binary Nanoparticle Superlattices. *Nature* **2006**, 439, 55–59.
- (76) Stampfli, P. A Dodecagonal Quasiperiodic Lattice In Two Dimensions. *Helv. Phys. Acta* 1986, 1260–1263.
- (77) Baake, M.; Klitzing, R.; Schlottmann, M. Fractally Shaped Acceptance Domains of Quasiperiodic Square-Triangle Tilings with Dedecagonal Symmetry. *Phys. A* **1992**, *191*, 554–558.
- (78) Xiao, C.; Fujita, N.; Miyasaka, K.; Sakamoto, Y.; Terasaki, O. Dodecagonal Tiling in Mesoporous Silica. *Nature* **2012**, *487*, 349–353
- (79) Alexander, S.; McTague, J. Should All Crystals Be Bcc? Landau Theory of Solidification and Crystal Nucleation. *Phys. Rev. Lett.* **1978**, 41, 702–705.
- (80) Zhang, C.-Z.; Wang, Z.-G. Random Isotropic Structures and Possible Glass Transitions in Diblock Copolymer Melts. *Phys. Rev. E* **2006**, 73, 031804.
- (81) Leocmach, M.; Tanaka, H. Roles of Icosahedral and Crystal-like Order in the Hard Spheres Glass Transition. *Nat. Commun.* **2012**, *3*, 974.
- (82) Royall, C. P.; Williams, S. R. The Role of Local Structure in Dynamical Arrest. *Phys. Rep.* **2015**, *560*, 1–75.
- (83) Ediger, M. D.; Angell, C. A.; Nagel, S. R. Supercooled Liquids and Glasses. *J. Phys. Chem.* **1996**, *100*, 13200–13212.
- (84) Jónsson, H.; Andersen, H. C. Icosahedral Ordering in the Lennard-Jones Liquid and Glass. *Phys. Rev. Lett.* **1988**, *60*, 2295–2298
- (85) Dzugutov, M. Formation of a dodecagonal quasicrystalline phase in a simple monatomic liquid. *Phys. Rev. Lett.* **1993**, *70*, 2924–2927.
- (86) Roth, J.; Denton, A. R. Solid-Phase Structures of the Dzugutov Pair Potential. *Phys. Rev. E* **2000**, *61*, 6845–6857.
- (87) Lifshitz, R.; Diamant, H. Soft quasicrystals-Why are they stable? *Philos. Mag.* **2007**, *87*, 3021–3030.
- (88) Iacovella, C. R.; Keys, A. S.; Glotzer, S. C. Self-Assembly of Soft-Matter Quasicrystals and Their Approximants. *Proc. Natl. Acad. Sci. U.S.A.* **2011**, *108*, 20935–20940.
- (89) Klatt, M. A.; Lovri, J.; Chen, D.; Kapfer, S. C.; Schaller, F. M.; Schönhöfer, P. W. A.; Gardiner, B. S.; Smith, A.; Schröder-turk, G. E.;

- Torquato, S. Universal Hidden Order in Amorphous Cellular Geometries. *Nat. Commun.* **2019**, *10*, 811.
- (90) Jeon, S.; Jun, T.; Jo, S.; Ahn, H.; Lee, S.; Lee, B.; Ryu, D. Y. Frank-Kasper Phases Identified in PDMS-b-PTFEA Copolymers with High Conformational Asymmetry. *Macromol. Rapid Commun.* **2019**, *40*, 1900259.
- (91) Shoemaker, C. B.; Shoemaker, D. P. Concerning Systems for the Generating and Coding of Layered, Tetrahedrally Close-Packed Structures of Intermetallic Compounds. *Acta Crystallogr., Sect. B: Struct. Crystallogr. Cryst. Chem.* 1972, 28, 2957–2965.
- (92) Takagi, H.; Yamamoto, K. Phase Boundary of Frank-Kasper σ Phase in Phase Diagrams of Binary Mixtures of Block Copolymers and Homopolymers. *Macromolecules* **2019**, *52*, 2007–2014.
- (93) Ungar, G.; Zeng, X. Frank-Kasper, quasicrystalline and related phases in liquid crystals. *Soft Matter* **2005**, *1*, 95–106.
- (94) Zhang, R.; Zeng, X.; Ungar, G. Direct AFM Observation of Individual Micelles, Tile Decorations and Tiling Rules of a Dodecagonal Liquid Quasicrystal. *J. Phys.: Condens. Matter* **2017**, 29, 414001.
- (95) Ungar, G.; Percec, V.; Zeng, X.; Leowanawat, P. Liquid Quasicrystals. *Isr. J. Chem.* **2011**, *51*, 1206–1215.
- (96) Zhang, W.; Lu, X.; Mao, J.; Hsu, C.-H.; Mu, G.; Huang, M.; Guo, Q.; Liu, H.; Wesdemiotis, C.; Li, T.; et al. Sequence-Mandated, Distinct Assembly of Giant Molecules. *Angew. Chem., Int. Ed.* **2017**, 56, 15014–15019.
- (97) Holerca, M. N.; Sahoo, D.; Partridge, B. E.; Peterca, M.; Zeng, X.; Ungar, G.; Percec, V. Dendronized Poly(2-oxazoline) Displays within only Five Monomer Repeat Units Liquid Quasicrystal, A15 and σ Frank-Kasper Phases. *J. Am. Chem. Soc.* **2018**, *140*, 16941–16947.
- (98) Dutour Sikirić, M.; Delgado-Friedrichs, O.; Deza, M. Space Fullerenes: A Computer Search for New Frank-Kasper Structures. *Acta Crystallogr., Sect. A: Found. Crystallogr.* **2010**, *A66*, 602–615.